Supporting Information

Section A: Pourbaix Theory

The iron Pourbaix diagram was used to determine key phase information on ionized metals in solution as a function of pH, temperature, and constituent concentration.

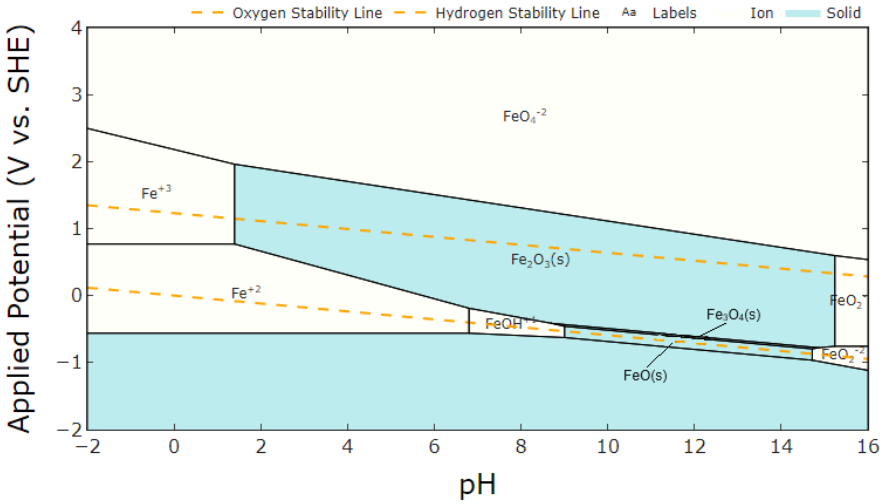

Figure SA1: Iron Pourbaix diagram, generated using The Materials Project database.[1]

The definition of applied potential (E) is given by the Nernst Equation (Equation 1), wherein E^o is the standard electrode potential of a certain ion, R is ideal gas constant, T is temperature, n is the total moles of electrons transferred during the electrochemical exchange, and F is Faraday's constant.[2]

$$Applied\ Potential = E = E^o - \frac{RT}{nF} \ln\left(\prod \frac{[products]}{[reactants]}\right) \quad \text{(Equation 1)}$$

Further, the Gibb's free energy (ΔG) of Fe^{n+} ionization (Equation 2) indicates ion stabilization in aqueous solution is only possible for ions with a positive standard electrode potential (E^o) under given synthetic conditions.

$$\Delta G = -nFE^o \quad \text{(Equation 2)}$$

Section B: MIL-100(Fe) Recipe and pH Spectrum Design

MIL-100(Fe) was prepared via the following literature procedure with some modification.[3] 2.26 g of iron(II)chloride tetrahydrate ($FeCl_2 * 4H_2O$, Sigma Aldrich) was mixed with 96.76 ml of distilled deionized water (DDI). The resulting solution was allowed to stir for one hour before its further use. 1M NaOH (Goodrich Chemical Enterprise) was prepared in a Teflon container (Parr Instrument Company) to avoid mineral leaching from glassware under caustic conditions. 1.59 g of BTC linker ($C_6H_3(CO_2H)_3$, Sigma Aldrich) was dissolved using 23.71 g of 1M NaOH and likewise allowed to stir for at least one hour. After stirring, the pHs of the solutions were approximately 3.5 and 9.5 respectively, as measured by a Lab 855 pH meter (SI Analytics). Under room temperature conditions, the linker solution was next added dropwise continuously over the course of about ten minutes. The initial pH of the mixture was measured to be approximately 5. Time zero was taken after the completion of linker dropwise addition. A brown precipitate was immediately observed. The nucleation reaction was allowed to proceed for 4 hours, after which the precipitate was collected using centrifugation. The MIL-100(Fe) powder was rinsed three times by vortex mixing with DDI and once by mixing with ethanol (Aik Moh Paints and Chemicals Pte Ltd). The particles were finally fully isolated using vacuum filtration through a 0.1 μm PVDF Durapore filter (Merck) and dried for 12 hours in a 100^{o}C vacuum oven.

To vary the pH of synthesis, molar ratios of precursors were altered and the pH of resulting solution was measured, as detailed in Table SA1 below.

Table SB1: Precursor molar ratio modifications for systematic pH variance. BTC linker remains in excess in all cases.

pH Solution Mix	$FeCl_2 * 4H_2O$ (mmol)	BTC (mmol)	NaOH (mmol)	H_2O (mmol)
5.0	1.5	1	3	880
2.3	1.5	2	3	880
8.5	1.5	1	6	880
5.7	1.5	0.5	3	880
4.1	1.5	1	1.5	880

Section C: Supporting SEM, TGA Decomp, and FTIR

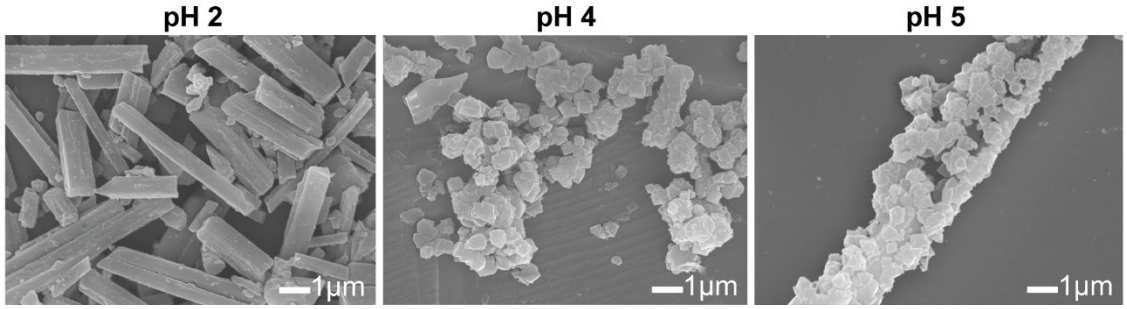

Figure SC1: SEM images of indicated sample precipitate.

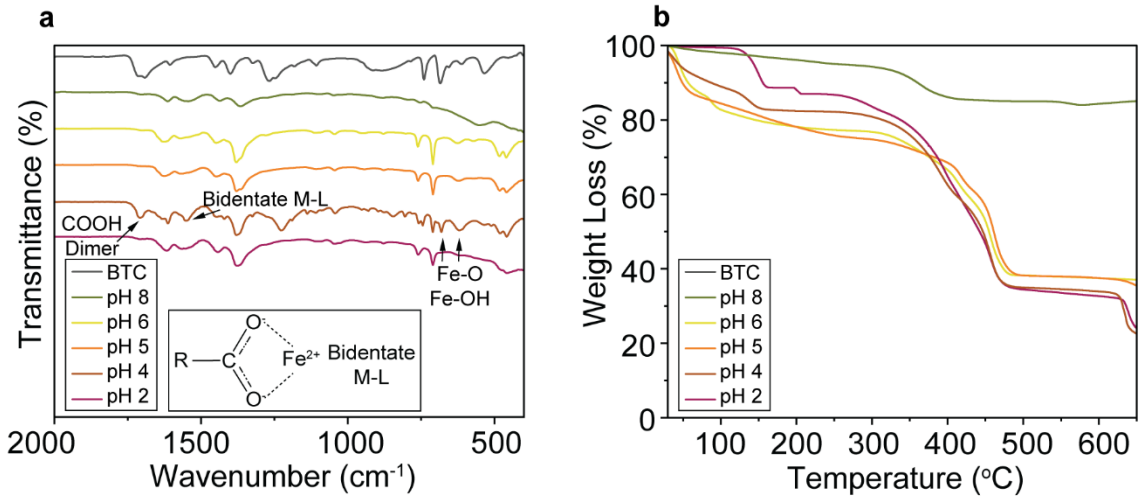

Figure SC2: Identification of sample impurities via FTIR and thermal decomposition. (a) FTIR spectra of sample precipitate generated at given pH, (b) TGA decomposition curves of the same.

FTIR spectral peaks located around 620 cm^{-1} are attributed to Fe-O stretching, with Fe-O-H deformations present in low pH samples indicative of iron hydroxide formation.[4-6] At pH 4 and below, carboxylic acid functionalities on the BTC linker had yet to be fully deprotonated, leading to increased interaction between Fe^{3+} nodes, generated by redox potential shift from their Fe^{2+} precursor, and -OH species in solution to maintain charge balancing. Furthermore, below the pH of complete acidic dissociation (4.70), hydrogen bonding between COOH dimers also encouraged Fe-OH bonding.[7] Suboptimal bidentate cation-carboxylate coordination, noted at 1550 cm^{-1}, was present at pH 4.[4] The thermodynamic equilibrium established at pH 4 therefore encourages linker dimer formation under room temperature conditions. Reduced M-L complexation gave rise to bidentate species, explaining the absence of highly crystalline MIL-100(Fe) at pH 4 and room temperature.

Thermal decomposition of all samples below 200°C is attributed to release of entrapped moisture and residual solvent.[8] Between 350°C and 500°C, the organic BTC linker decomposed, and above 600°C, complete decomposition of the metal species occurred.[9] The absence of sample

mass decline arising from Fe decomposition in samples synthesized above pH 8 again indicates iron oxide species were predominant, in agreement with XRD analysis.[10] Next, product phase uniformity was preliminarily characterized based on the number of decomposition steps observed. The presence of varied metal-ligand (M-L) interactions arising from byproducts such as FeOOH, Fe^{2+}-BTC, etc., in samples generated below pH 5 was evidenced by additional decomposition steps between 150°C and 300°C. An average of 5.7% difference in mass loss was observed when comparing pH 4 and pH 5 samples within this temperature range, attributed the thermal breakdown of Fe^{2+} impurities, while between pH 5 and 6, a 1.4% average difference was observed. The reduced difference in mass loss around pH 5 is consistent with the earlier XRD finding that pure phase MIL-100(Fe) is formed under room temperature conditions at pH 5.

Section D: UV-vis Absorbance Conversion and Analysis

Absorbance calculations were performed using the Kubelka-Munk Function (Equation 3). In the function, K refers to the absorption coefficient of the sample, and S is the scattering coefficient.

$$f(r_\infty) = \frac{(1-r_\infty)^2}{2r_\infty} = \frac{K}{S} \quad \text{(Equation 3)}$$ [11]

Due to our small particle size, specular reflected light effects were deemed negligible when using diffused reflected light. Sample thicknesses were equivalent given careful filling of the powder sample specific sample holder for 60-mm Integrating Sphere (Shimadzu).

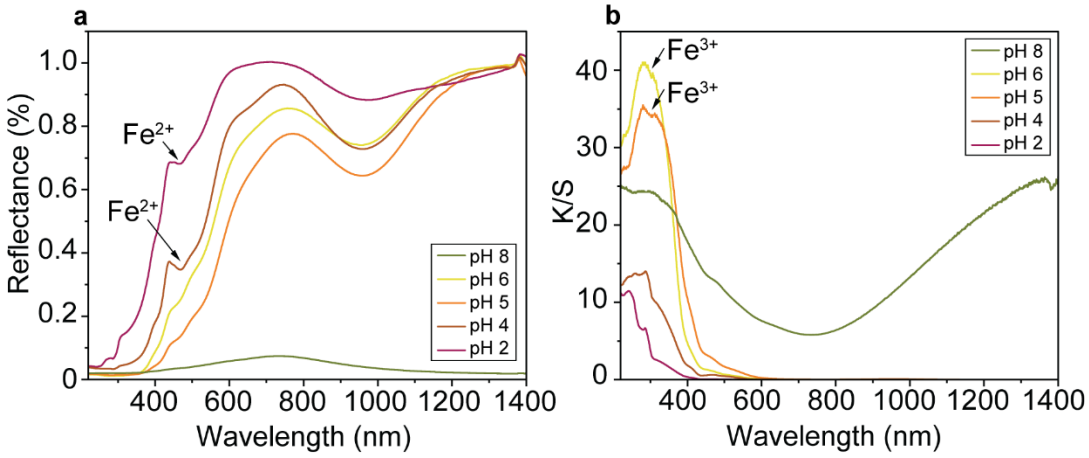

Figure SD1: Full spectra UV-vis data. Spectral reflectance for indicated samples over the complete instrument working range; (a) reflectance data, (b) absorbance data. Spectra were collected using a Shimadzu powdered sample holder with quartz window, and standard barium sulfate background.

Section E: Ligand Field Theory

Ligand field theory was employed in our analysis and based on Equation 4, where *E* represents the energy of visible light photons.

$$E = hv = h\frac{c}{\lambda} \qquad \text{(Equation 4)}\ [12]$$

Here, *h* is equal to Plank's constant (6.626 x10^{-34} J*s), ν is frequency in Hertz (s^{-1}), *c* is the speed of light within a vacuum (2.99E8 m/s), and λ is the photon's wavelength.

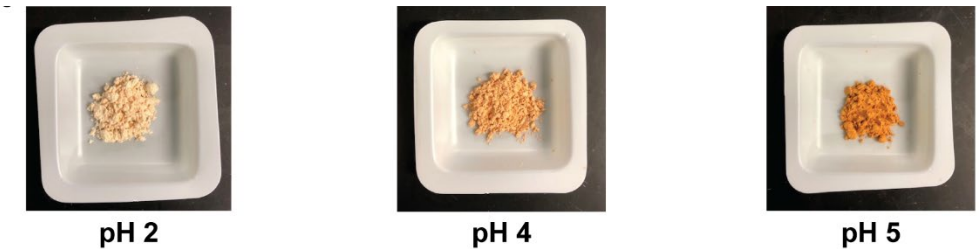

Figure SE1: Examples of powder sample optical color differences based on indicated synthetic pH.

Muted color expression at pH ≤ 4 is explained by the d-orbital splitting behavior of iron-ligand complexations. Based on the magnitude of d-orbital splitting, Δ_o, also known as the crystal field splitting energy, high spin or low spin transition complexes may be formed. With increase in electrostatic charge (e.g., $Fe^{3+} > Fe^{2+}$), the strength of interactions between metal and ligand during complex formation increases the magnitude of Δ_o. Photons of visible light, with energy *hv*, excite the electrons of Fe^{3+} complexes into the higher energy d-orbitals by overcoming the crystal field splitting energy. The probability of excitation is reduced in Fe^{2+} complexes due to the prohibitive spin pairing energy, resulting in muted color expression and suggesting the increased presence of Fe^{2+} cations.[13]

Section F: XPS Fitting

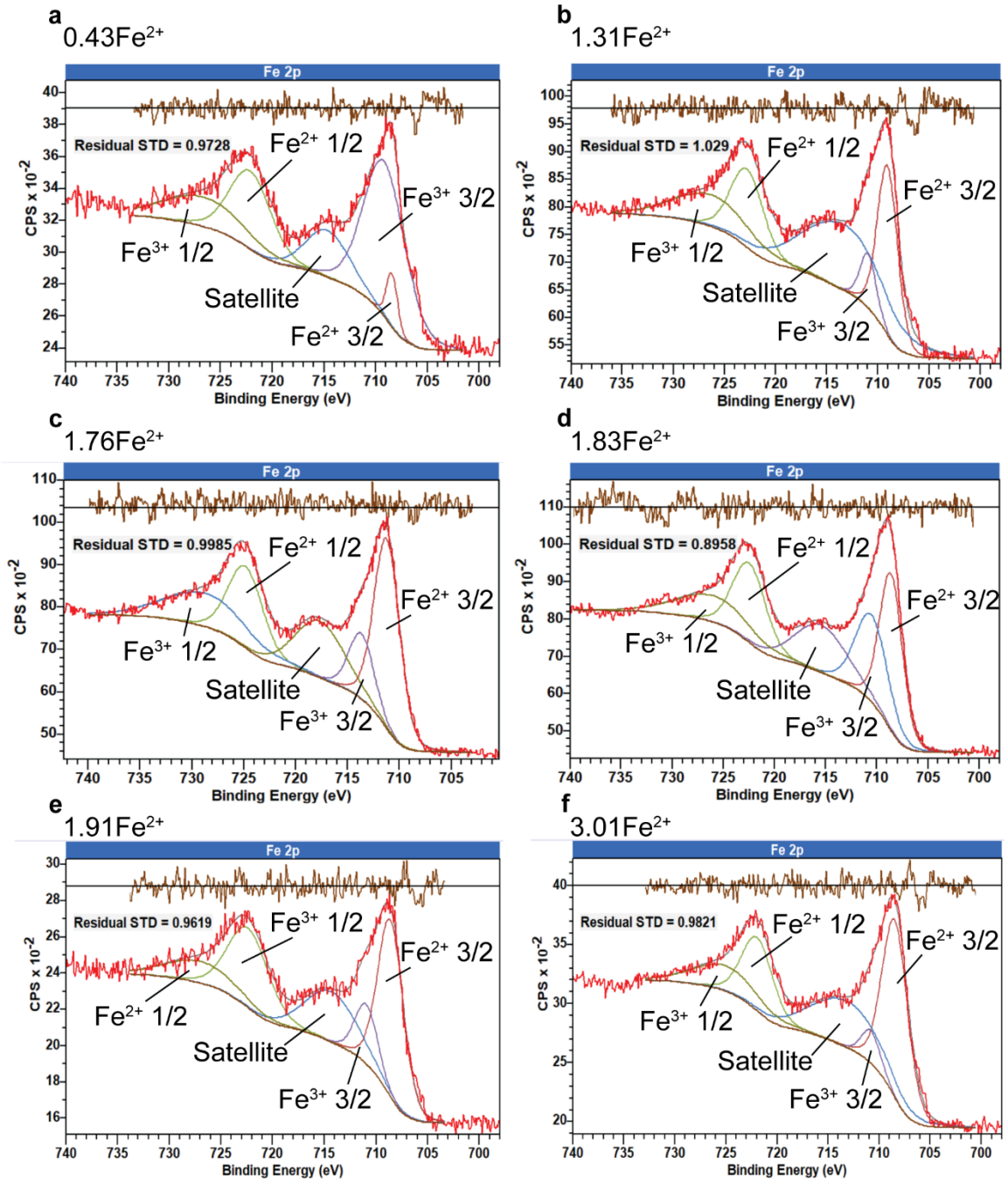

Figure SF1: Supporting XPS. Fe 2p orbital deconvolution for $x\mathrm{Fe}^{2+}$ samples (a) $x = 0.43$ (b) $x = 1.31$, (c) $x = 1.76$, (d) $x = 1.83$, (e) $x = 1.91$, (f) $x = 3.01$.

Table SF1: Deconvolution Fitting Peak Areas Determined by CasaXPS.[14]

Sample	Orbital Spin Species	Area (CPSeV)
0.43Fe^{2+}	2p 3/2 2^{+}	475
	2p 3/2 3^{+}	5114
	2p 1/2 2^{+}	2581
	2p 1/2 3^{+}	1918
1.31Fe^{2+}	2p 3/2 2^{+}	12276
	2p 3/2 3^{+}	9512
	2p 1/2 2^{+}	8986
	2p 1/2 3^{+}	6674
1.76Fe^{2+}	2p 3/2 2^{+}	14536
	2p 3/2 3^{+}	8239
	2p 1/2 2^{+}	84967
	2p 1/2 3^{+}	4847
1.83Fe^{2+}	2p 3/2 2^{+}	7894
	2p 3/2 3^{+}	2005
	2p 1/2 2^{+}	5957
	2p 1/2 3^{+}	5571
1.91Fe^{2+}	2p 3/2 2^{+}	3163
	2p 3/2 3^{+}	940
	2p 1/2 2^{+}	2262
	2p 1/2 3^{+}	1073
3.01Fe^{2+}	2p 3/2 2^{+}	4928
	2p 3/2 3^{+}	660
	2p 1/2 2^{+}	2487
	2p 1/2 3^{+}	1803

Section G: Defect XRD Peak Intensity Ratios

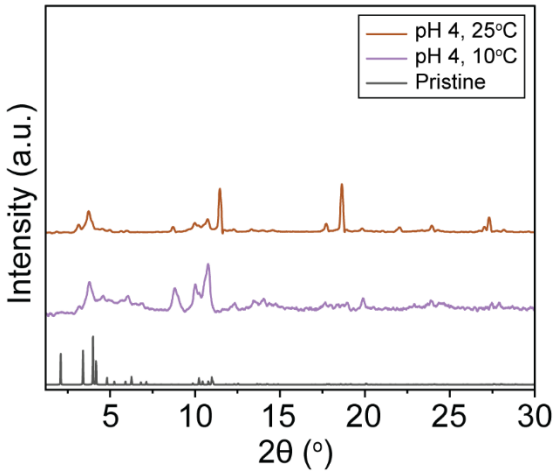

Figure SG1: XRD spectra of non-MIL-100(Fe) pH 4 samples.

Table SG1: Relative ratios of leading XRD spectra as a reflection of defects. Missing linker/cluster and neat spectra derived from CrystalMaker 10/CrsytalDiffract 6 simulation.

Spectra	111	220	311
Missing linker pent cage	0.2	1	0.6
Missing cluster pent cage	0.2	0.9	1
Missing linker hex cage	1	0.3	0.6
Missing cluster hex cage	1	0.4	0.5
Pristine	0.6	0.7	1
$0.43Fe^{2+}$	0.5	0.6	1
$1.31Fe^{2+}$	0.7	0.8	1
$1.76Fe^{2+}$	0.9	0.9	1
$1.83Fe^{2+}$	0.5	0.7	1

Section H: Supporting Sorption Performance (BET)

Henry's Law constants were determined via the initial slope method.[15] Linear fits of CO_2 and N_2 adsorption data, collected via BET at 25°C, were taken in the low-pressure regime below 300 mmHg. Taking a ratio of the Henry's Law constants (the initial slope of the CO_2 adsorption curve over that of N_2) gave the selectivity values. Henry's Law can be expressed via Equation 5.

$$n_i = k_i P_i$$ (Equation 5)[15]

Where n_i is the quantity of gaseous component i adsorbed, and P_i is the partial pressure of the gas phase, which is equavalent to the absolute analysis pressure when pure gas is dosed for analysis.

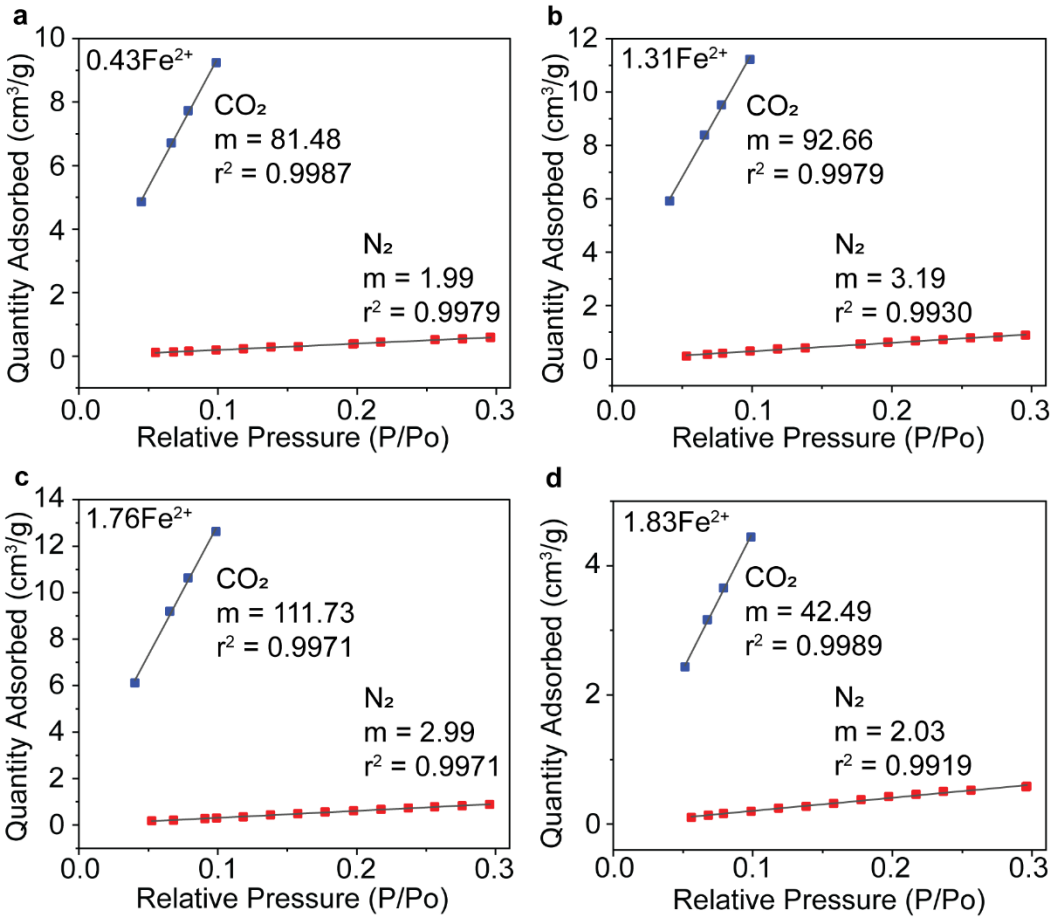

Figure SK1: Henry's regimes used in selectivity calculations. BET sorption results at 25°C and linear curve fittings for xFe^{2+} samples (a) x = 0.43 (b) x = 1.31, (c) x = 1.76, (d) x = 1.83.

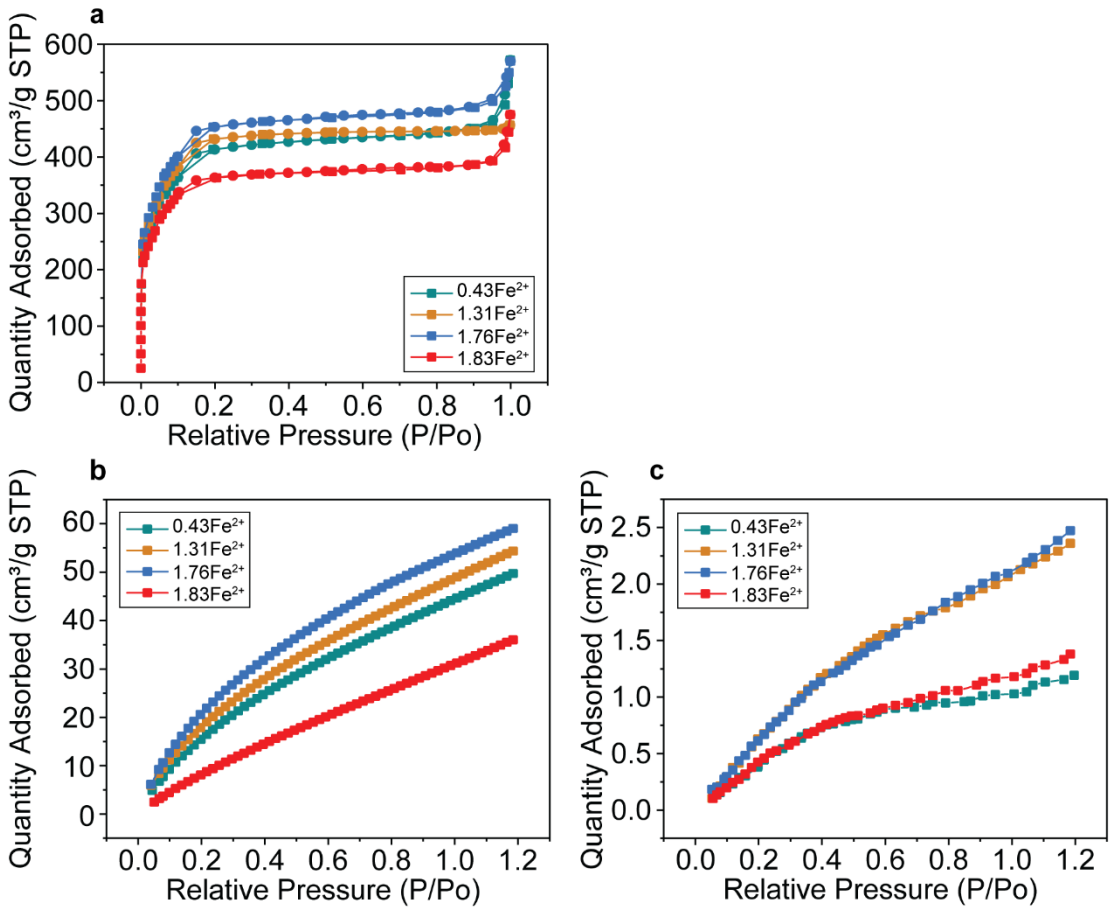

Figure SK2: Complete adsorption performance data. (a) BET 77K nitrogen isotherms of indicated samples, (b) complete CO_2 and (c) N_2 absorption 25°C isotherms.

Heat of adsorption metrics were calculated at the point of zero coverage using the Clausius-Clapeyron equation (Equation 6) within the Micrometrics BET software. CO_2 adosrption curves collected at 25°C and 15°C were utilized to perform the calculations.

$$\ln\left(\frac{P_1}{P_2}\right) = \frac{\Delta H_{ads}}{R}\left(\frac{1}{T_2} - \frac{1}{T_1}\right) \qquad \text{(Equation6)}^{[16]}$$

P_1 and P_2 represent the pressure of initial CO_2 adsorption (at the point of zero coverage) for curves collected at T_1 = 25°C and T_2 = 15°C respectively. ΔH_{ads} is the heat of adsorption and R is the ideal gas constant.

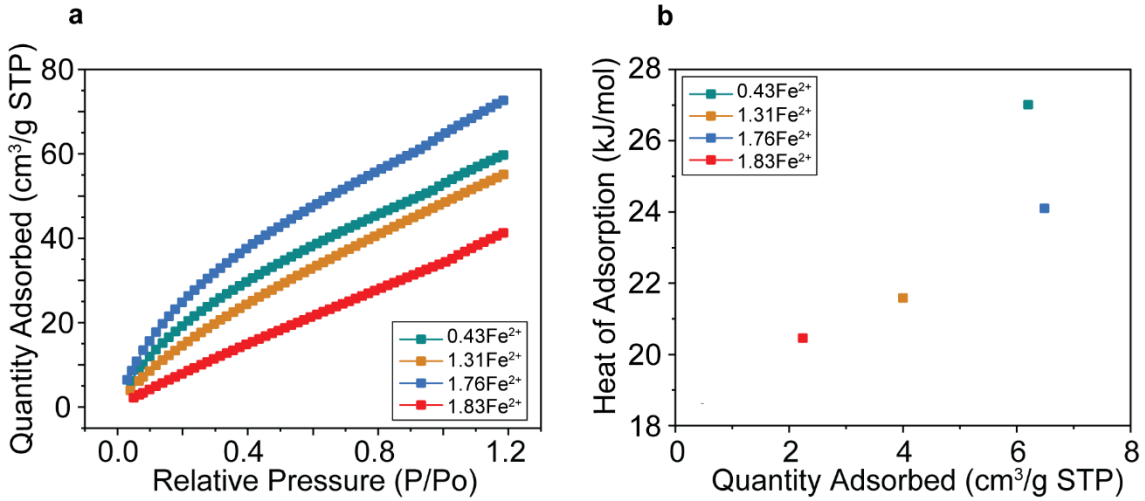

Figure SK3: Heat of adsorption curves and values at zero coverage. (a) BET 15°C CO_2 uptake isotherms of indicated samples, (b) calculated heat of adsorption values at zero coverage.

References

1. Aqueous Stability (Pourbaix). The Materials Project, US Department of Energy, https://next-gen.materialsproject.org/pourbaix (accessed May 2023).
2. M. M. Walczak, D. A. Dryer, J. Dana D, M. G. Foss and N. T. Flynn, *Journal of Chemical Education*, 1997, **74**, 1195.
3. K. Guesh, C. A. D. Caiuby, A. l. Mayoral, M. Díaz-García, I. Díaz and M. Sanchez-Sanchez, *Crystal Growth and Design*, 2017, **17**, 1806-1813.
4. E. R. Encina, M. Distaso, R. N. K. Taylor and W. Peukert, *Crystal Growth and Design*, 2015, **15**, 194-203.
5. A. Espina, M. V. Cañamares, Z. Jurašeková and S. Sanchez-Cortes, *ACS Omega*, 2022, **7**, 27937-27949.
6. A. G. Roca, J. F. Marco, M. a. d. P. Morales and C. J. Serna, *Journal of Physical Chemistry C*, 2007, **111**, 18577-18584.
7. Y.-K. Seo, J. W. Yoon, J. S. Lee, U.-H. Lee, Y. K. Hwang, C.-H. Jun, P. Horcajada, C. Serre and J.-S. Chang, *Microporous and Mesoporous Materials*, 2012, **157**, 137-145.
8. L. Feng, K. Y. Wang, G. Day, M. Ryder and H. C. Zhou, *Chemical Reviews*, 2020, **120**, 13087-13133.
9. K. Mondal, H. Lorethova, E. Hippo, T. Wiltowski and S. B. Lalvani, *Fuel Processing Technology*, 2004, **86**, 33-47.
10. X. Ding, L. Bao, J. Jiang and H. Gu, *RCS Advances*, 2014, **4**, 9314-9320.

11. *UV Talk Letter Vol 14: Diffuse Refectance Measurement of Powder Samples and Kubelka-Munk Transformation*, Report C101-E137, Shimadzu Coorperation 2014.
12. N. J. Tro, *Chemistry: A Molacular Approach*, Pearson, 4th edn., 2017.
13. C. J. Jones, *d- and f-Block Chemistry*, RSC Publishing, Cambridge, United Kingdom, 2002.
14. N. Fairley, V. Fernandez, M. Richard-Plouet, C. Guillot-Deudon, J. Walton, E. Smith, D. Flahaut, M. Greiner, M. Biesinger, S. Tougaard, D. Morgan and J. Baltrusaitis, *Applied Surface Science Advances*, 2021, **5**.
15. A. L. Myers and J. M. Prausnitz, *AIChE Journal*, 1965, **11**, 121-126.
16. M. Li, J. N. Hall, K. Fleming and P. Bollini, *Energy Fuels*, 2022, **36**, 5816-5824.